

Article

Temperature and Humidity Profile Retrieval from FY4-GIIRS Hyperspectral Data Using Artificial Neural Networks

Xi Cai ^{1,2}, Yansong Bao ^{1,2,*}, George P. Petropoulos ³ , Feng Lu ⁴, Qifeng Lu ⁴, Liuhua Zhu ^{1,2} and Ying Wu ^{1,2}

¹ Collaborative Innovation Center on Forecast and Evaluation of Meteorological Disasters, CMA Key Laboratory for Aerosol-Cloud-Precipitation, Nanjing University of Information Science & Technology, Nanjing 210044, China; xcai@nuist.edu.cn (X.C.); zhulh@nuist.edu.cn (L.Z.); yingwu@nuist.edu.cn (Y.W.)

² School of Atmospheric Physics, Nanjing University of Information Science & Technology, Nanjing 210044, China

³ Department of Geography, Harokopio University of Athens, El. Venizelou 70, Kallithea, 17671 Athens, Greece; gpetropoulos@hua.gr

⁴ Key Laboratory of Radiometric Calibration and Validation for Environmental Satellites /National Satellite Meteorological Center, China Meteorological Administration, Beijing 100081, China; lufeng@cma.gov.cn (F.L.); luqf@cma.gov.cn (Q.L.)

* Correspondence: ysbao@nuist.edu.cn

Received: 20 April 2020; Accepted: 4 June 2020; Published: 9 June 2020



Abstract: This study proposes a new technique for retrieving temperature and humidity profiles based on Artificial Neural Networks (ANNs) using data acquired from the GIIRS (Geosynchronous Interferometric Infrared Sounder) L1 and ERA-Interim (European Centre for Medium-Range Weather Forecasts Reanalysis). The approach is also compared against another method that uses simulated data from the radiative transfer model to construct the retrieval network. Furthermore, the two methods of network construction are evaluated in the North China Plain for July and August 2018, for which ground validated observations concurrent to the satellite data were available. In summary, the results showed that: (1) the ANN built with the GIIRS L1 and the EC data is superior to that built with the forward simulation and EC data in retrieval accuracy; (2) the retrieval accuracy for the troposphere exceeds that for the stratosphere; (3) the root mean square errors (RMSEs) of the relative humidity in the troposphere as retrieved by the two ANNs are 6.003% and 10.608%, respectively; (4) a relatively low correlation (R) between the simulated and observed radiance of the GIIRS is found, ranging between 720 and 736.875 cm^{-1} , and the correlation between the simulated and observed radiance of the water vapor channels exceeds that between the temperature channels; (5) compared with Atmospheric Infrared Sounder's (AIRS') products, our retrieved temperature profiles exhibit preferable consistency and the humidity retrievals also show an acceptable accuracy. Our study offers important insights towards improving our ability to retrieve atmospheric temperature and humidity profiles from the most sophisticated Earth Observation instruments such as the GIIRS of the FY-4 satellite, which could assist in expanding the use of those products globally.

Keywords: GIIRS; hyperspectral; Earth Observation; Artificial Neural Network; temperature; humidity; profile

1. Introduction

Information on atmospheric temperature and humidity profiling is indispensable for describing the thermal and dynamic states of the atmosphere. Accurate data of those parameters are of great

significance for improving the accuracy of numerical weather prediction [1] and in short-term weather warning and forecasting [2]. Although ground data are essential for meteorological research, those have, inherent, a number of limitations, which make them impractical and not cost-effective to use for this purpose. In the recent decades, research on atmospheric, temperature and humidity profile retrieval, exploiting contemporary technologies such as Earth Observation (EO), has made great progress [3]. In this respect, EO data acquired particularly from meteorological satellites can effectively supplement regions lacking in conventional observation data [4].

The first investigations concerned with the development of techniques to detect atmospheric parameters using satellite EO data began in the middle of last century [5]. Since then, there has been a rapid evolution in optical sensing devices and infrared hyperspectral remote sensing detection [6]. In order to achieve higher vertical resolution detection, NASA has built a new generation of global environmental monitoring system, named the National Polar-orbiting Operational Environmental Satellite System Preparatory Project (NPP). The latter gives clear requirements for satellite atmospheric temperature and humidity detection (Table 1) [7,8].

Table 1. Observation requirements of atmospheric sounding from the National Polar-orbiting Operational Environmental Satellite System Preparatory Project (NPP).

Observation Accuracy (Root Mean Square Error)			Vertical Resolution
Height Range	Temperature	Humidity	
Surface to 500 hPa	1 K	10%	0.3~0.5 km/layer
500~300 hPa	1 K	10%	0.5~1 km/layer
300~100 hPa	1 K	20%	1~2 km/layer
Above 100 hPa	1 K	-	2~3 km/layer

On 11 December 2016, the second generation of China's geostationary weather satellite, FY-4, was successfully launched. It is equipped with the Geosynchronous Interferometric Infrared Sounder, GIIRS, which can perform high-precision quantitative detection of atmospheric structure in the vertical direction. This feature is not available in any other geostationary orbit meteorological satellite in Europe and America [9]. In an approach similar to IASI and CrIS, the Geosynchronous Interferometric Infrared Sounder (GIIRS) onboard the FengYun-4 (FY-4) series [10] is a Fourier transform spectrometer based on a classic Michelson instrument [11]. It is also the first time that the "Four-Dimensional observation" of the atmosphere has been realized in geostationary orbit in the world [12].

Given the developments in hyperspectral remote sensing and on-orbit operation of infrared hyperspectral sensors (such as the Atmospheric Infrared Sounder (AIRS), IASI and CrIS), methods of retrieving atmospheric temperature and humidity profiles utilizing information from satellite EO systems are constantly developing [3]. At present, the main retrieval methods include statistical regression, physical and statistical-physical methods [3]. In some studies, an eigenvector statistical method is used to retrieve the temperature and humidity profiles of the Atmospheric Infrared Sounder (AIRS). The results from those studies have shown that the hyperspectral atmospheric vertical sounder can improve the retrieval accuracy for the upper and middle troposphere and tropopause [13–15].

Ma et al. [16] used the eigenvector statistical method to obtain the initial atmospheric profile and then used the nonlinear Newton iteration method to further improve the retrieval accuracy. Guan, Ren, Bao, Lu, Liu and Xiao [3] found that the Metop-A /IASI infrared hyperspectral data can be used for the high-precision detection of atmospheric temperature and water vapor mixing ratio profiles based on the one-dimensional variational method. Guan et al. [17] used the observation data of the AIRS for retrieval. Their results showed that the artificial neural network (ANN) algorithm and the eigenvector statistical method are comparable in terms of calculation time and accuracy. Jiang et al. The authors in [18] demonstrated the use of a neural network algorithm to retrieve the atmospheric temperature profile from AIRS data; the vertical resolution of the tropospheric temperature retrieval

results reached 1 km. Shi et al. [19] developed the SCENE algorithm (Stochastic Cloud clearing, followed by Eigenvector radiance compression and denoising, followed by Neural network Estimation) and used it to retrieve the temperature and humidity profiles from the Atmospheric Infrared Sounder (AIRS) and Advanced Microwave Sounding Unit (AMSU). The retrieval results show that the SCENE algorithm has higher retrieval accuracy compared with the AIRS secondary product algorithm. It also requires significantly less computation at the same time, which makes it suitable for the fast retrieval of geophysical parameters. Fully considering the influence of carbon dioxide, clouds and high surface elevations, Blackwell and Chen [20] developed different neural networks for three classifications of surface elevations in order to derive temperature and humidity profiles from High-resolution Infrared Radiation Sounder (HIRS) observations. The long-term effect of the increase in carbon dioxide on HIRS temperature sounding channel measurements is accounted for in the retrieval algorithm. The retrieval results of the algorithm indicate that there is a close correlation between the retrievals and radiosonde as well as the Global Positioning System Radio Occultation (GPS-RO) observations. Bao, Cai, Qian, Min, Lu and Zuo [1] used the BP (Back Propagation) neural network to retrieve the atmospheric temperature profiles from the ground-based microwave (MW) radiometer. Authors compared their results with the sounding data and level 2 products of the microwave radiometer. Their results indicated that the range of the temperature RMSE was 1.0~2.0 K. Following up this study, Bao, Wang, Chen, Zhou, Dong and Min [8] used a BP neural network to study the atmospheric temperature retrieval method for the simulated data of the FY-4 vertical sounder GIIRS. The authors reported an RMSE of the retrieved tropospheric temperature in China within 1 K. These researchers and also others (e.g., Wang et al. 2014a) argued that although the statistical regression inversion algorithm is simple in calculation and stable in retrieval process, it does not consider the atmospheric radiation transmission process, and the retrieval accuracy is to be further improved [8,21]. The variational method considers the process of atmospheric radiation transmission, and can retrieve the vertical distribution information of atmospheric temperature and humidity [22,23]; however, it is an inconvenient approach in modeling, and an initial field, a large amount of calculation and continuous iteration are required. The ANN does not need the complex relationships of physical models, nor does it need great effort to find a formula for retrieving variables. However, it can describe the non-linear relation between radiance and atmospheric variables and is very convenient to use. Therefore, ANNs were usually used to develop operational systems [1,24]. All the above studies provide strong evidence for the potential of ANNs in temperature and humidity profile retrieval from EO data. However, to our knowledge, presently, there is a lack of studies focusing on the retrieval of temperature and humidity profiles from FY-4 vertical sounder GIIRS, one of the latest and most sophisticated instruments currently in orbit.

In this context, the present study aims at covering this gap by proposing a new method for performing the fast and accurate retrieval of temperature and humidity profiles utilizing FY4 GIIRS EO data, used synergistically with an ANN algorithm. This approach is also compared against a different method of constructing a network with the simulated data for temperature and humidity profile retrieval. Furthermore, the two network construction methods are evaluated in the North China Plain for July and August 2018 for which ground validated observations concurrent to the satellite data were available. The practical use of our developed method is demonstrated herein for retrieving temperature and humidity profiles in the North China Plain.

2. Study Area and Datasets

2.1. Study Area

The North China Plain is one of the three major plains in China and denotes the second largest plain in China. The territory ranges from 32°N to 40°N and 114°E to 121°E. It exhibits a warm temperate monsoon climate with distinct season variation, and it is cold and dry in winter. The North China Plain exhibits a relatively flat and less complex terrain, with a well-developed transportation network, and it has been the political, economic and cultural center of China since ancient times. Although the area of

the North China Plain only accounts for 7.26% of the national area, it carries 25.12% of the national population and 35.98% of the motor vehicles. The consumption of coal fuel and gasoline account for 33.48% and 7.11% of the national total, respectively, contributing 30.58% of the national GDP [25]. The area has been at the focal point of many research studies in recent years [25–28]. Compared with other regions, the uniform flat terrain in this region makes it easier to carry out the forward simulation of the FY4-RTM model with fewer terrain factors to be considered, so as to compare the results with the methods proposed by us.

2.2. GIIRS Data

In our study, Level 1 data of the GIIRS vertical sounder as well as the (European Centre for Medium-Range Weather Forecasts Reanalysis) ERA-Interim data are used as the input data of the ANN. The GIIRS denotes the first hyperspectral infrared atmospheric vertical sounder onboard a geostationary weather satellite. Its on-orbit spatial resolution is 16 km, each detector has 32×4 sensor elements, and the frequency of observation for specific targets is more than 20 times per day [29]. The interferometric atmospheric vertical sounder has more than 1600 detection channels; the obtained vertical distribution of atmospheric temperature and humidity can provide wide-range, continuous, rapid and accurate remote sensing information for weather forecasting. Table 2 denotes the parameters and main detection purposes of the GIIRS. The GIIRS L1 data were collected from 1 July 2018 to 31 August, in the North China Plain (32°N – 40°N , 114°E – 121°E).

Table 2. Geosynchronous Interferometric Infrared Sounder (GIIRS) sensor specifications.

		FY-4A GIIRS		
		Wave Band (cm^{-1})	Spectral Resolution (cm^{-1})	Number of Channels
Spectral Parameters	Long Wave Infrared (LWIR)	700~1130	0.625	689
	Mid Wave Infrared (MWIR)	1650~2250	0.625	961
	Visible light	0.55~0.75 μm		1
Spatial Resolution	LWIR/SWIR/MWIR	satellite bottom point 16 km		
	Visible light	satellite bottom point 2 km		
Detection Area	China region	$5000 \times 5000 \text{ km}^2$		
	Meso-small scale	$1000 \times 1000 \text{ km}^2$		
Temporal Resolution	China region	<1 h		
	Meso-small scale	<1/2 h		
Main Detection Purposes of Different Wave Bands	700–790 cm^{-1}	With respect to temperature profile detection, using the sensitivity to cold targets and cloud top heights to retrieve temperature profiles in the presence of partial clouds		
	790–1130 cm^{-1}	Surface and cloud features, O_3 detection		
	1210–1650 cm^{-1}	Water vapor and temperature profile detection; N_2O , CH_4 , and SO_2 detection		
	2100–2150 cm^{-1}	Total amount of carbon monoxide		
	2150–2250 cm^{-1}	Temperature profile detection, total amount of N_2O		

The GIIRS data were downloaded from the website of the FengYun-SAI (Scientific Algorithm Innovation) (www.fysai.com). Level 1 data of the GIIRS for other time periods are also available at no cost from the National Satellite Meteorological Centre (<http://satellite.nsmc.org.cn/PortalSite/Data/Satellite.aspx>).

The ERA-Interim data are available four times a day at 00:00, 06:00, 12:00 and 18:00 UTC, but the GIIRS vertical sounder does not include observation data around 18:00 UTC every day. In order to

time-match the observations with the EC data, the GIIRS data were collected at 00:00, 06:00 and 12:00 UTC in July–August, 2018 within a 0.5 h time window for the GIIRS observations. Based on the detection purposes of different spectral bands of the GIIRS, channels within the range of $700\text{--}790\text{ cm}^{-1}$ are used as the input channels of the temperature retrieval network, and channels within the range of $1800\text{--}2000\text{ cm}^{-1}$ are used as the input channels of the humidity retrieval network.

2.3. ERA-Interim Data

The ERA-Interim data have a spatial resolution of $0.125^\circ \times 0.125^\circ$. They contain information on the atmospheric temperature, humidity, ozone and cloud cover at 37 altitudes from 1000 hPa to 1 hPa. The data were collected at 00:00, 06:00 and 12:00 UTC every day from the ECMWF public datasets (<https://apps.ecmwf.int/datasets/>). In order to match the observation data of the GIIRS, the time range is also from July to August 2018, and the data region is also the North China Plain ($32^\circ\text{N}\text{--}40^\circ\text{N}$, $114^\circ\text{E}\text{--}121^\circ\text{E}$). Using the sea surface temperature data, the data points on the ocean surface are removed and the data points on the land surface are retained, considering the surface consistency and that the ocean area does not belong to the North China Plain. Based on the total cloud cover in the surface data set, the cloudy data points are removed and the clear sky data points are retained. The distribution of the clear sky data points in July and August 2018 after time-space matching is shown in Figure 1.

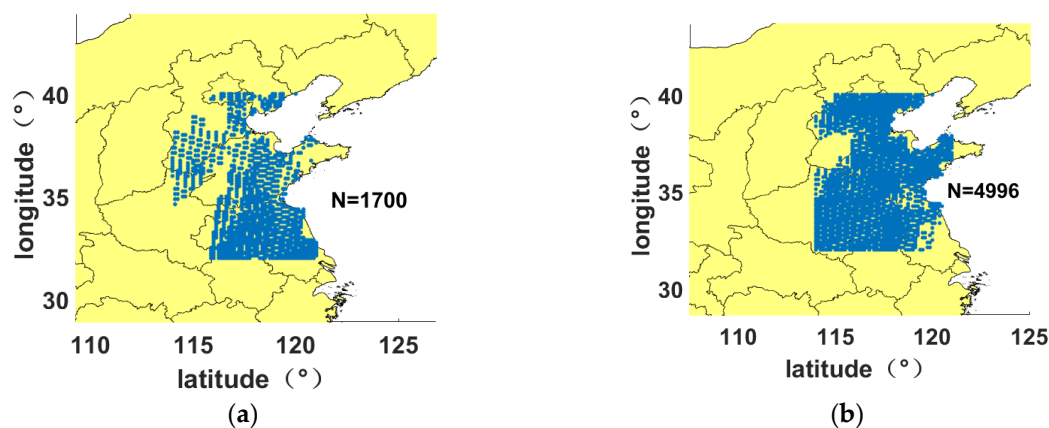


Figure 1. Distribution of clear sky data points used in the study in the North China Plain throughout July and August 2018. (a) Distribution of the clear sky data points used in the study in the North China Plain throughout July; (b) Distribution of the clear sky data points used in the study in the North China Plain throughout August (blue dots represent sample points).

3. Methods

3.1. Data Pre-Processing

The GIIRS L1 data and the ERA-Interim data are first pre-processed, and data points located on the ocean in the data region are removed by using the sea surface temperature data in the EC surface data set. Subsequently, based on the total cloud cover data in the EC surface data set, the cloudy data points are removed and the clear sky data points are retained. The retained EC data are matched with the GIIRS observation data in time and space. The spatial matching requires that the distance between them should not be greater than 10 km, and the nearest data point meeting the requirement is selected as the matching data. The samples are then divided. In order to avoid interrelation between samples and adjacent samples, the first three of every five samples are used for training, and the last two are used for testing. Therefore, 60% of the samples are used as training samples, and the remaining 40% are used for the test data. Given the effect of view zenith angle [30], an angle correction is performed on the samples prior to the construction of the network and retrieval to decrease the effect of the view

zenith angle on the retrieval results. For this purpose, the radiance value of each channel of each sample is multiplied by the cosine value of the satellite zenith angle of the sample.

3.2. Method Implementation

This section is concerned with the description of the method of directly using EC data and GIIRS observation data to build the ANN network, i.e., the newly proposed method of this study. In addition, this approach is compared to the method of first using the profile data for forward simulation and then using the forward simulation data to build the network. The latter method can still obtain enough samples through numerical simulation to construct a retrieval network when the observation data are insufficient. This is also an approach that has been widely used in previous studies [8,17] compared with the method proposed herein. Thus, the two methods for network construction are compared in this study and their differences are quantitatively evaluated. The two methods of network construction are evaluated in the North China Plain for July and August 2018 for which ground validated observations concurrent to the satellite data were available. For convenience, from this point onwards, the former method is referred to as “Method 1” and the latter, as “Method 2”. Figure 2 shows the methodology in the present study.

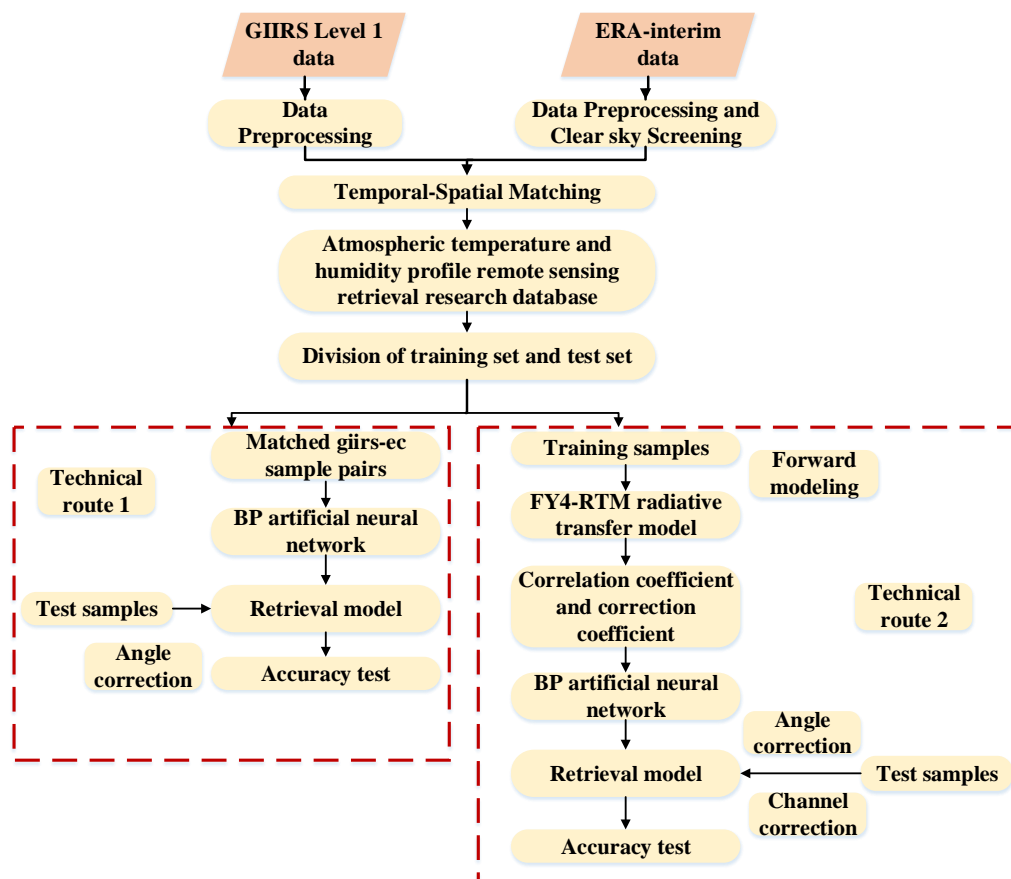


Figure 2. Methodology implementation in the present study.

With respect to Method 1, i.e., the proposed method of directly constructing a network by using EC data and GIIRS observation data, an angle correction is performed on the training dataset based on the divided dataset, and the network is trained with the training dataset. The test data are inserted into the network for temperature and humidity retrieval after the angle correction. The input part of the network denotes the observed radiance data of the GIIRS, and the output part of the network denotes the temperature and relative humidity profile data at 37 altitudes.

With respect to Method 2, i.e., the method of using EC data first for forward simulation and then using the forward simulation data and EC data to build the network, the EC data in the training set are processed and formatted. Then, they are used in the FY4-RTM model for numerical simulation to obtain the simulated GIIRS radiance data. After the apodization of the measured GIIRS data, the simulated GIIRS radiance data are compared with the measured data of the GIIRS. Samples with a low correlation coefficient (R) and large root mean square error (RMSE) (see Section 3.4.5) are removed. With respect to the retained data, the correlation coefficient between the simulated and observed radiance and correction coefficient of each channel are calculated, and correction models for each channel are constructed. After the angle correction of the simulated GIIRS radiance data, the simulated GIIRS radiance data are used as the input, and the corresponding EC data are used as the output of the network to build the network. The test data are initially processed by apodization and then inserted into the network for retrieval after angle and channel correction.

3.3. FY4-RTM Radiative Transfer Model

Usually, an accurate and fast radiative transfer model (RTM) is required to simulate radiances with specific atmosphere profiles for applications of satellite-based infrared (IR) radiances for Numerical Weather Prediction (NWP) [11]. In order to compare Method 1 with Method 2, the FY4-RTM radiative transfer model is used in this study. The model is a radiative transfer model used to calculate the radiance of sensors in the case of cloud and rain. Simultaneously, it can also be used for radiance simulation under clear sky conditions by changing its internal parameters [8]. The radiance under specified conditions is obtained by editing and modifying the internal program file, compiling, and running on the Linux system. The fast algorithm PFAAST (Pressure layered Fast Atmospheric Transmittance) employed in the model is based on the work of S.Hannon, L.Strow and W.McMillan [31]. It is suitable for various instruments, including hyperspectral instruments with variable resolution.

The model requires, as inputs, both atmosphere and surface parameters. The atmosphere parameters include 101 layers (0.005–1100 hpa) of atmospheric temperature, water vapor and ozone information; the surface parameters include surface temperature and surface pressure. The default surface pressure is set to the bottom pressure level, the surface skin temperature is defined as the last level of the temperature profile, and the surface emissivity is set to 0.98 for all bands. These values can be modified by the users inside “fy4stbc.f”.

3.4. BP Neural Network Model

3.4.1. Network Structure

Neural networks (NNs) are nonlinear function approximators trained to infer a statistical relationship between inputs and outputs from a training ensemble using a few parameters, without requiring direct knowledge of the functional input/output relationship [32–38]. They are composed of simple computing elements termed as nodes that are interconnected [39–41]. When compared to linear fitting, the ANN exhibits a significantly stronger fitting capability when the data relationship is nonlinear [34,42–45]. Furthermore, one of the benefits of using ANNs is that uncertainties in the input data are accounted for during the training process of the neural network. Indeed, ANNs are relatively insensitive to reasonable uncertainties in the input data [46] and they do not require an accurate mathematical model [47], and thus, they are easy to program and calculate with hardware and software [48]. In today’s meteorological field, an increasing number of neural network methods have been introduced in precipitation forecast, fog forecast and temperature and humidity profile retrieval research [49]. The network consists of an input layer, a hidden layer and an output layer, which can be effectively used for the approximation of complex nonlinear functions and the mapping of continuous functions with arbitrary precision.

3.4.2. Input and Output Layers of the Network

Once a certain ANN architecture is determined, it has to be trained with an input–output data set to adjust its weights in order to generate output as similar as possible to the true output [45]. With respect to Method 1 and based on the detection purposes of different spectral bands of the GIIRS, the 145 channels located in the range of 700–790 cm^{-1} are used as the input nodes of the temperature retrieval network and the 321 channels located in the range of 1800–2000 cm^{-1} are used as the input nodes of the humidity retrieval network; the temperature and relative humidity values of the EC data at 37 levels are used as output nodes. With respect to Method 2, based on the above, 24 channels located in the range of 700–790 cm^{-1} and 14 channels located in the range of 1800–2000 cm^{-1} are removed for the poor consistency between simulation and observation.

3.4.3. Implicit Layer Settings of the Network

The performance of the network is affected by the number of nodes in the hidden layer. A low number of nodes in the hidden layer leads to insufficient information. Many nodes in the hidden layer increase training time and affect work efficiency [50]. A series of comparative tests on the different number of hidden layer nodes are performed before the training of the network. On this basis, in the temperature retrieval test, based on relevant literature [51,52] and the Kolmogorov theorem and by considering the calculation efficiency and retrieval accuracy, the number of hidden layer nodes is finally determined as 291 for Method 1 and 243 for Method 2, and the calculation formula is as follows:

$$N_{\text{hid}} = 2N_{\text{in}} + 1 \quad (1)$$

where N_{hid} denotes the number of hidden layer nodes and N_{in} denotes the number of input layer nodes.

In the humidity retrieval test, Equation (1) is found to be not quite suitable for the humidity retrieval network, and the number of hidden layer nodes calculated is too large. Based on the empirical formula obtained by Zhang and Li [51] on the basis of a large number of experimental results, the number of hidden layer nodes is finally determined as 179 for Method 1 and 172 for Method 2, and the formula is as follows:

$$N_H = \frac{N_I + (N_O, N_C)_{\text{max}}}{2} \quad (2)$$

where N_H denotes the number of hidden layer nodes, N_I denotes the dimension of the input vector, N_O denotes the number of output nodes, N_C denotes the number of target classifications, and $(N_O, N_C)_{\text{max}}$ denotes the maximum values of N_O and N_C . In the study, there is no such variable as N_C , so the value of the $(N_O, N_C)_{\text{max}}$ is determined as N_O .

3.4.4. Transfer Function and Training Algorithm of the Network

The performance of the neural network is related to the overall structure of the network and also affected by the selection of transfer function and training algorithm. In the retrieval network, Tansig, a hyperbolic tangent S-type transfer function, is used between the input layer and hidden layer, and between the hidden layer and output layer. This expresses the non-linear relationship between the nodes well and is not affected by the input value, and its output value is defined between -1 and 1 . We compare the performance of several typical fast learning algorithms. Given a large number of training data and complex network parameter settings, the network training algorithm is determined as a scaled conjugate gradient method, trainscg [53]. This approach is suitable for function fitting and pattern classification, with fast convergence and stable performance, especially suitable for large-scale networks. This approach is considered as an excellent local search method; it is not only one of the most useful methods for solving large-scale linear equations but also one of the most effective algorithms for solving large-scale nonlinear optimization problems.

3.4.5. Evaluation Methods

Four statistical metrics are employed to evaluate, quantitatively, the retrieval accuracy of the model, namely the correlation coefficient (R), mean square error (MSE), root mean square error ($RMSE$) and mean bias error (MBE , written as ME in the figures), as expressed below:

$$MSE = \frac{1}{n} \sum_{i=1}^n (x_i - y_i)^2 \quad (3)$$

$$R = \frac{\sum_{i=1}^n (x_i - \bar{x})(y_i - \bar{y})}{\sqrt{\sum_{i=1}^n (x_i - \bar{x})^2 \sum_{i=1}^n (y_i - \bar{y})^2}} = \frac{\sum_{i=1}^n x_i y_i - n\bar{x}\bar{y}}{\sqrt{(\sum_{i=1}^n x_i^2 - nx^2)(\sum_{i=1}^n y_i^2 - ny^2)}} \quad (4)$$

$$RMSE = \sqrt{MSE} \quad (5)$$

$$MBE = \frac{1}{n} \sum_{i=1}^n (x_i - y_i) \quad (6)$$

In the above equations, n denotes the number of sample profiles, x_i denotes the temperature or relative humidity value retrieved by the neural network and y_i denotes the temperature or relative humidity value of the EC data.

4. Results

4.1. Retrieval Results of Method 1

With respect to Method 1, 4018 training samples in July and August 2018 are used to train the network and establish the retrieval model, and the remaining 2678 test samples are used to test the network to verify the accuracy of the retrieval model.

4.1.1. Temperature Retrieval Results

Figure 3 shows the scatter diagram of the retrieved atmospheric temperature. The number of test samples is 2678, and the vertical pressure ranges from 1000 to 1 hPa, with a total of 37 layers. The data are collected from July 2018 to August in the North China Plain (32°N–40°N, 114°E–121°E). The results show that the correlation coefficient between the retrieved temperature and target temperature value is 0.999; the RMSE of the atmospheric temperature of the whole layer is 0.629 K. The MBE is -0.014 K, thereby implying that the retrieved temperature is generally 0.014 K lower than the target temperature. The retrieved and target temperature values are evenly distributed on both sides of the $y = x$ line.

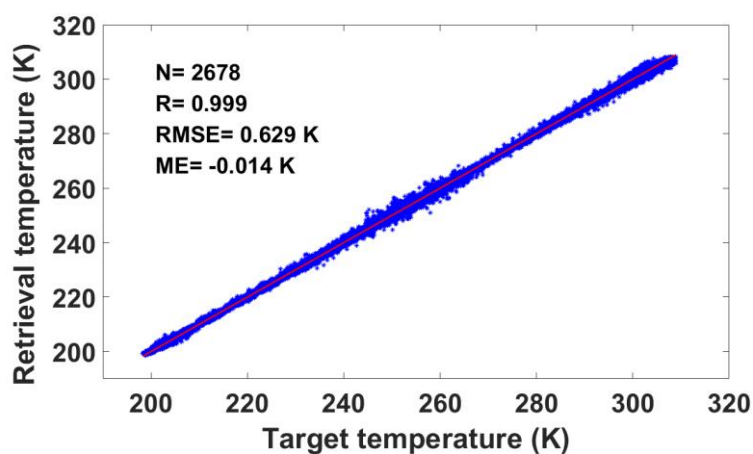


Figure 3. Scatter diagram of temperature retrieval results based on Method 1.

Figure 4 shows the distribution of the RMSE and MBE of the temperature retrieval in the troposphere and stratosphere. As shown in Figure 4a,b, the average RMSE in the troposphere is 0.557 K, and the

RMSE in each layer is less than 1 K in the troposphere. The lowest RMSE occurs at 550 hPa, which is 0.418 K; and the highest RMSE occurs at 1000 hPa, which is 0.961 K. The MBE of troposphere is of the order of 0.1 K, the maximum positive deviation is 0.012 K, and the maximum negative deviation is -0.094 K. The curve is approximately distributed on both sides of the standard line. As shown in Figure 4c,d, the average RMSE in the stratosphere is 0.769 K, which slightly exceeds that of the troposphere. The RMSE in most of the atmospheric layers is still within 1 K, and slightly higher at the top of the stratosphere with a maximum value of 1.301 K. The MBE of the stratosphere is also in the order of 0.1 K, which is distributed on both sides of the standard line.

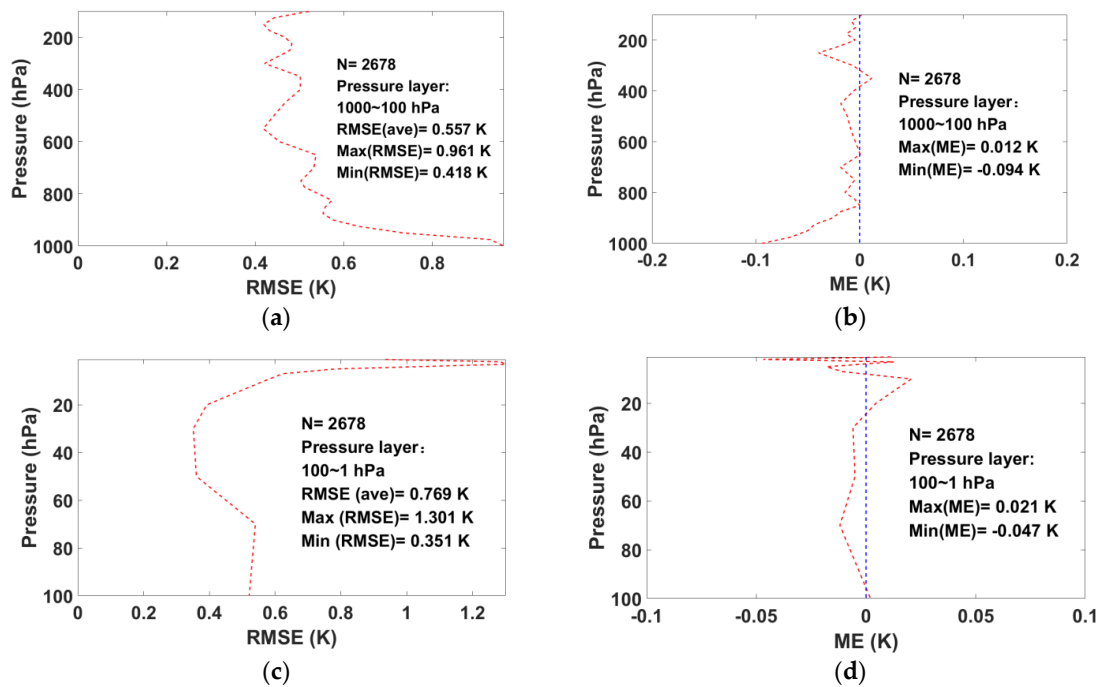


Figure 4. Root mean square error (RMSE) and mean bias error (MBE) distribution of the temperature retrieval in the troposphere and stratosphere based on Method 1: (a) RMSE distribution map of the troposphere; (b) MBE distribution map of the troposphere; (c) RMSE distribution map of the stratosphere; (d) MBE distribution map of the stratosphere.

The samples shown in Figure 5 are the best sample case and the worst sample case in all the retrieval samples. As shown in Figure 5a, the best sample case is located at 34.375°N , 116.625°E in North China, on 24 August 2018, at 12:00 UTC. As shown in the figure, the retrieved temperature profile and target temperature profile exhibit preferable coherence and fit well at the temperature change corner. The correlation coefficient between the retrieved and target temperature is 0.999, the RMSE between the retrieved temperature value and target temperature value is 0.169 K, and the MBE is 0.001 K. The worst sample case is located at 34.25°N , 120.125°E in North China, on 9 August 2018, at 00:00 UTC. As shown in the figure, the retrieved temperature profile and target temperature profile exhibit poor coherence at the top of the stratosphere, and the RMSE between the retrieved temperature value and target temperature value reaches 2.213 K.

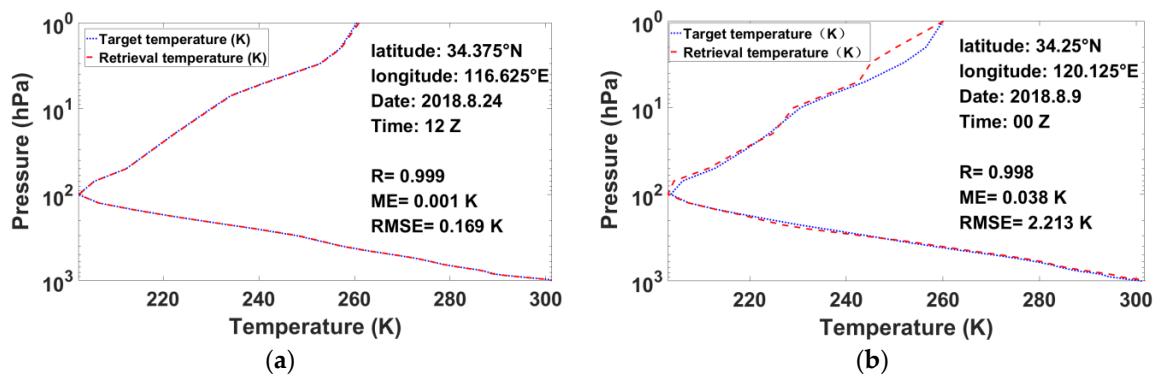


Figure 5. Diagram illustrating the temperature retrieval cases based on Method 1: (a) best case; (b) worst case.

4.1.2. Relative Humidity Retrieval Results

Figure 6 shows the scatter diagram of the retrieved atmospheric relative humidity. The number of test samples is 2678, and the pressure layer ranges from 1000–1 hPa, also exhibiting a total of 37 layers. The data time and region are consistent with the above study. The results indicate that the correlation coefficient between the retrieved relative humidity and the target relative humidity is 0.979. The RMSE of the relative humidity of the whole atmosphere is 5.133%, which is within 6%. The MBE is -0.008% , thereby implying that the retrieved relative humidity is 0.008% lower than the target relative humidity. The retrieved relative humidity and target relative humidity are evenly distributed on both sides of $y = x$ line.

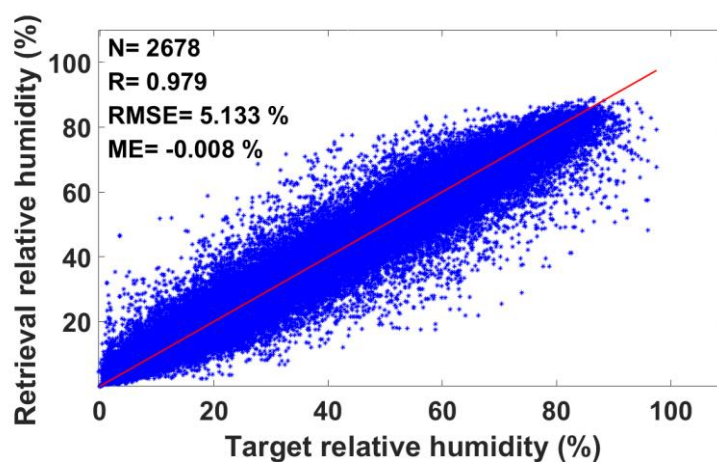


Figure 6. Scatter diagram of relative humidity retrieval based on Method 1.

Figure 7 shows the RMSE and MBE distribution of the relative humidity retrieval in the troposphere and stratosphere. As shown in Figure 7a,b, the average RMSE in the troposphere is 6.003%, and the RMSE in each layer within the troposphere is less than 8%. The lowest RMSE occurs at 100 hPa, which is 3.556%. The highest RMSE occurs at 225 hPa, which is 7.939%. The MBE in the troposphere is within $\pm 0.5\%$, the maximum positive deviation is 0.252%, and the maximum negative deviation is -0.347% ; the curve is approximately distributed on both sides of the standard line.

As shown in Figure 7c,d, the average RMSE in the stratosphere is 1.145%. When compared with the troposphere, the RMSE in the stratosphere is significantly decreased. The relative humidity in the upper layer is generally small because the water vapor content in the upper layer is far less than that in the surface layer, which leads to a rapid decrease in the RMSE above the troposphere, and it gets closer to 0% with the increase in height. The MBE of stratosphere is within $\pm 0.1\%$, and the retrieved relative humidity in the stratosphere is generally lower than the target relative humidity.

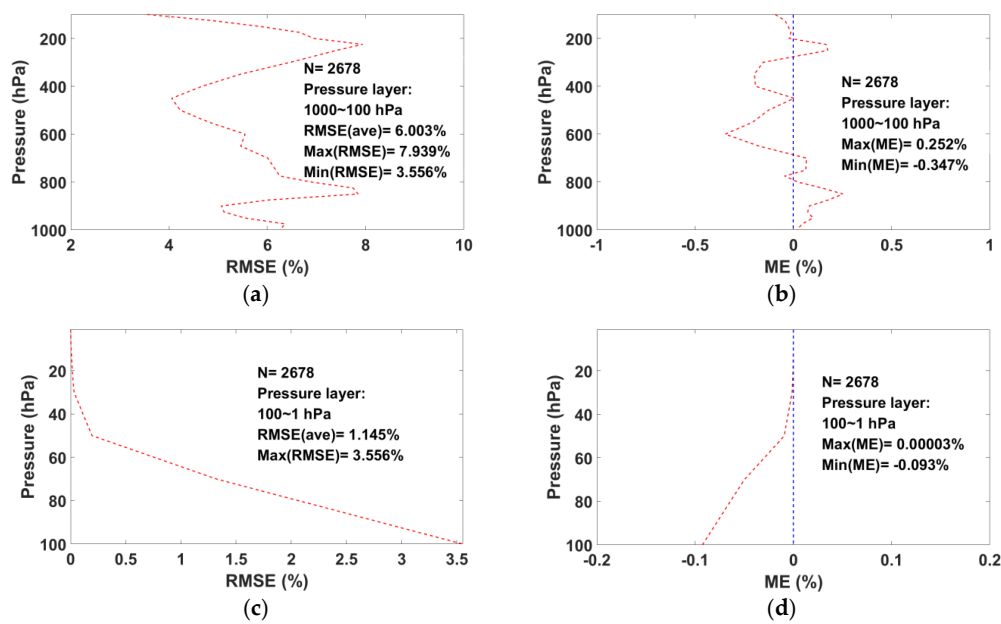


Figure 7. RMSE and MBE distribution of the relative humidity retrieval in the troposphere and stratosphere based on Method 1: (a) RMSE distribution map of the troposphere; (b) MBE distribution map of the troposphere; (c) RMSE distribution map of the stratosphere; (d) MBE distribution map of the stratosphere.

The samples shown in Figure 8 are the best sample case and the worst sample case in all retrieval samples. As shown in Figure 8a, the best sample case is in North China at 33.375°N, 117.125°E, and the data were measured on 24 August, 2018, at 00:00 UTC. As shown in the figure, the retrieved relative humidity profile is in good coherence with the target relative humidity profile, and they fit well at the relative humidity change corner. The correlation coefficient between the retrieved and target relative humidity is 0.999. The RMSE between the retrieved relative humidity value and target relative humidity value is 1.128%, while the MBE is 0.479%. The worst sample case is located at 40°N, 120°E in North China, on 16 August, 2018, at 06:00 UTC. As shown in the figure, there is a poor correlation between the retrieved relative humidity profile and the target relative humidity profile; the RMSE between the retrieved relative humidity value and target relative humidity value reaches 17.865%, and the MBE reaches 3.400%, thereby implying that the retrieved relative humidity is 3.400% higher than the target relative humidity.

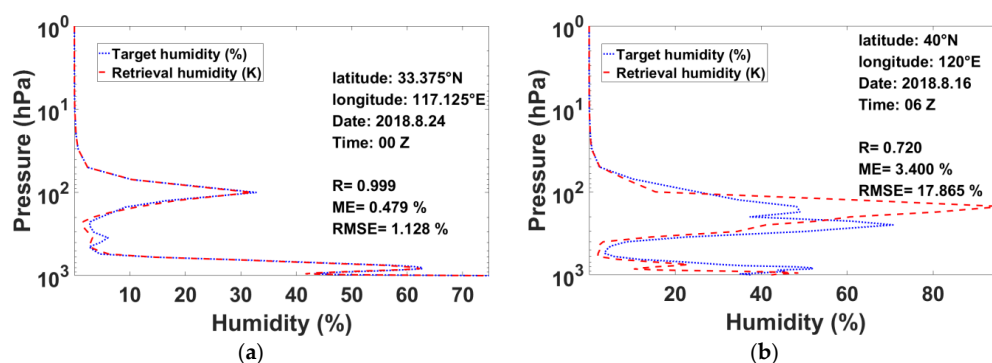


Figure 8. Diagram illustrating the relative humidity retrieval cases based on Method 1: (a) best case; (b) worst case.

4.2. Forward Simulation Results

With respect to Method 2, the divided training samples are used in the FY4-RTM model for simulation.

4.2.1. Simulated Sample Case

The simulated sample shown in Figure 9 is in the North China plain at 37.125°N, 119.250°E, on 24 August, 2018, at 12:00 UTC, with a satellite observation zenith angle of 45.698°. Figure 9a shows the comparison of the simulated and observed radiance over the whole band, Figure 9b shows a comparison diagram for the temperature band, and Figure 9c shows a comparison diagram for the humidity band where the blue curve denotes the simulated radiance, and green denotes the observed radiance. As shown in the figure, the simulated radiance curve and observed radiance curve of the GIIRS exhibit good coherence and overlap well. In the temperature band shown in Figure 9b, the RMSE between the simulation and observation is 2.748 mW/(m²·sr·cm⁻¹), and the simulated radiance is 0.674 mW/(m²·sr·cm⁻¹) higher than the observed radiance, on average. In the humidity retrieval band shown in Figure 9c, the RMSE between the simulation and observation is 0.395 mW/(m²·sr·cm⁻¹), and the simulated radiance is 0.237 mW/(m²·sr·cm⁻¹) higher than the observed radiance.

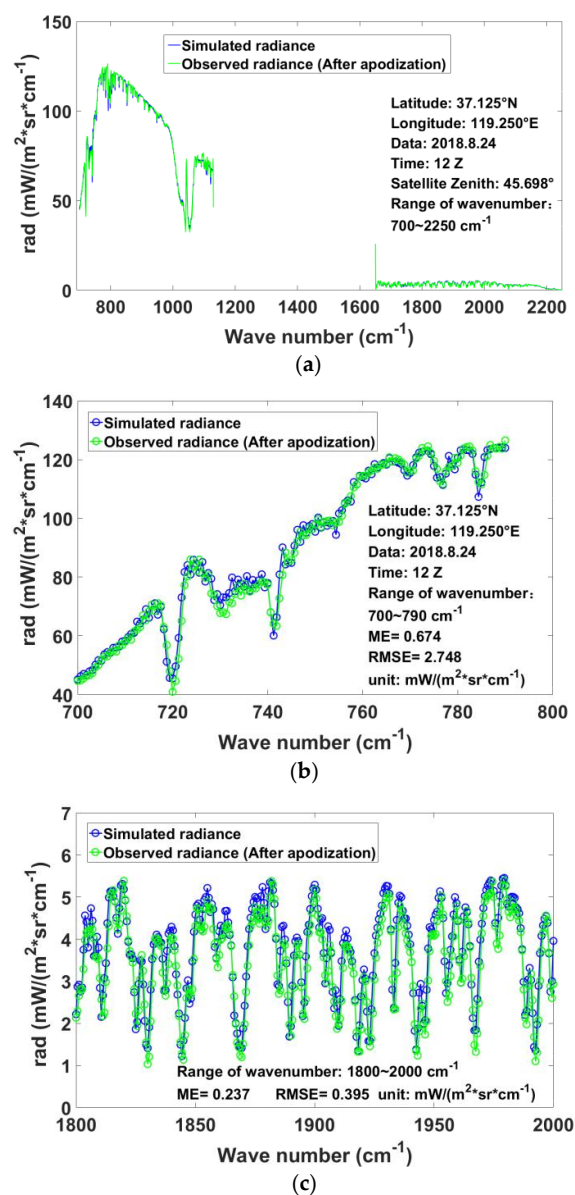


Figure 9. Forward simulation case diagram: (a) whole band comparison diagram; (b) temperature retrieval band comparison diagram; (c) humidity retrieval band comparison diagram (blue curve: simulated radiance; green curve: observed radiance).

4.2.2. Channel Correlation Coefficient Calculation

After the forward simulation, the corresponding GIIRS observation data are first processed by apodization and then compared with the simulated data. Samples with a significantly lower correlation coefficient and larger RMSE are eliminated, and the total number is 104. With respect to the remaining 3914 samples, the correlation coefficient between the simulated and observed radiance and correction coefficient of each channel are calculated, and the correction models for each channel are constructed. Figure 10 shows the statistics of the correlation coefficient between the simulated and observed radiance of the temperature and humidity retrieval channels. As shown in the figure, the average correlation coefficient of the 145 channels used for temperature retrieval is 0.751, and the correlation coefficient of most channels can reach 0.7 or above. Channels with a low correlation coefficient are concentrated in the wave number range of 720–736.875 cm^{-1} , and channels with a correlation coefficient of less than 0.7 are eliminated. After elimination, 121 channels for temperature retrieval network construction are obtained, as shown in Figure 10c. With respect to the humidity retrieval channels, the average correlation coefficient of the 321 channels is 0.852, which slightly exceeds that of temperature retrieval channels. In terms of distribution, the correlation coefficient of most channels is maintained at 0.75 or above. After the elimination of channels with correlation coefficient values of less than 0.75, 307 channels for humidity retrieval network construction are obtained, as shown in Figure 10d.

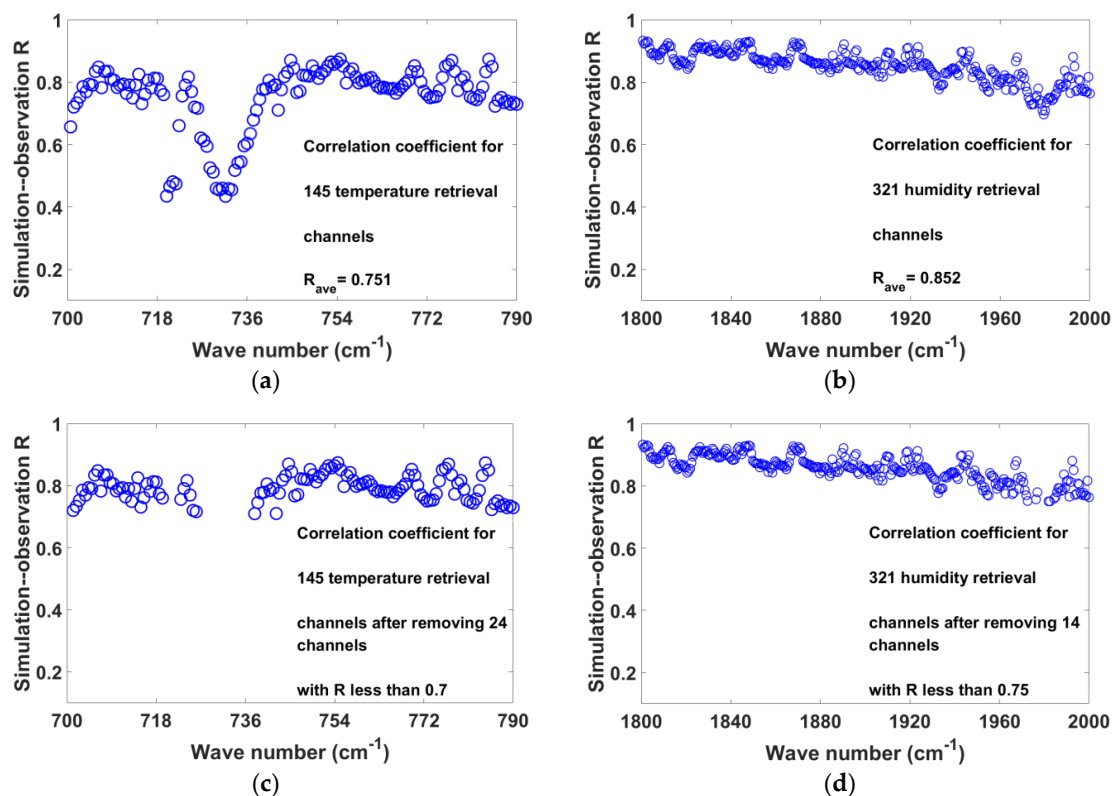


Figure 10. Correlation coefficient between the simulated and observed radiance of each channel: (a) correlation coefficient between the simulated and observed radiance of temperature retrieval channels; (b) correlation coefficient between the simulated and observed radiance of humidity retrieval channels; (c) correlation coefficient between the simulated and observed radiance of temperature retrieval channels after elimination; (d) correlation coefficient between the simulated and observed radiance of humidity retrieval channels after elimination.

4.2.3. Construction of Correction Model

As shown in the above correlation coefficients between the simulated and observed radiance diagram of each channel, a deviation exists between the measured radiance data of the GIIRS and

the simulated radiance data. In order to correct the deviation between the measured radiance and simulated radiance, the study obtains statistics of the correction coefficient between the measured and simulated radiance of each channel used for network construction and then constructs the correction model. In order to further improve the model accuracy and decrease the effect of other factors, sample points with the difference between the corrected and simulated radiances exceeding three times the root mean square error are eliminated, and the remaining sample points are used to reconstruct the correction model as the final correction model of the channel using the MATLAB function fitting tool. Figure 11 shows the correction model for some of the channels used for the network construction of temperature and humidity retrieval.

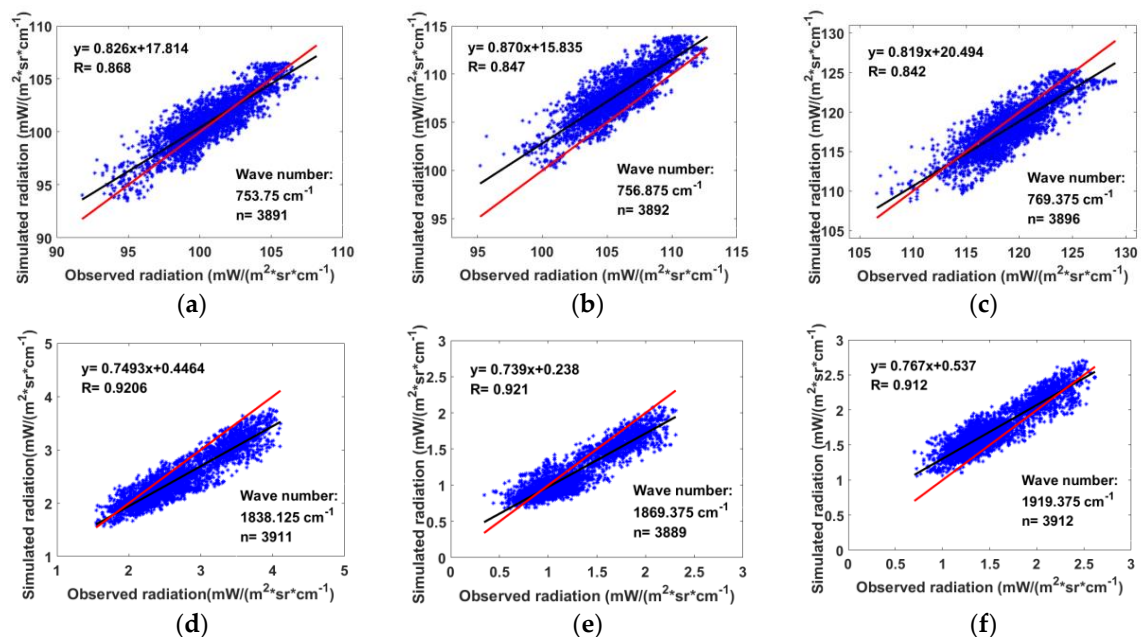


Figure 11. Correction model for partial channels used for the network construction of temperature and humidity retrieval: (a–c) correction model for partial channels used for the network construction of temperature retrieval; (d–f) correction model for partial channels used for the network construction of humidity retrieval (black line: the correction model; red line: the $y = x$ line).

4.3. Results of Method 2

4.3.1. Temperature Retrieval Results

The simulated GIIRS radiance data are used as the input of the network after angle correction, and the corresponding EC data are used as the output of the network in this method. The test data are initially processed by apodization and then inserted into the network for retrieval after angle and channel correction. Figure 12a shows the scatter diagram of the retrieved atmospheric temperature with Method 2. All the data information of the test samples is consistent with the above study. The results indicate that the correlation coefficient between the retrieval result and the target is 0.998. The RMSE of the atmospheric temperature of the whole layer is 1.703 K. The MBE is -0.04 K, and the retrieved temperature is generally 0.04 K lower than the target temperature.

Figure 12b,c show the distribution of the RMSE and MBE of the temperature retrieval in the troposphere and stratosphere. As shown in Figure 12b, the average RMSE in the troposphere is 1.527 K. Except for the bottom layer, the RMSE of each layer in the troposphere is less than 2 K, and it tends to decrease with an increase in height. The minimum RMSE value is 1.002 K at 150 hPa. The maximum RMSE is 2.288 K at 1000 hPa. The MBE curve of troposphere exhibits a slight variation around the reference line, and the absolute value of the maximum deviation does not exceed 0.25 K. As shown in Figure 12c, the average RMSE in the stratosphere is 2.048 K, which slightly exceeds that in the

troposphere. The RMSE in most of the layers is still within 2 K, and it slightly increases at the top of stratosphere, with a maximum value of 3.963 K. The absolute value of the maximum deviation is within the order of 0.1 K.

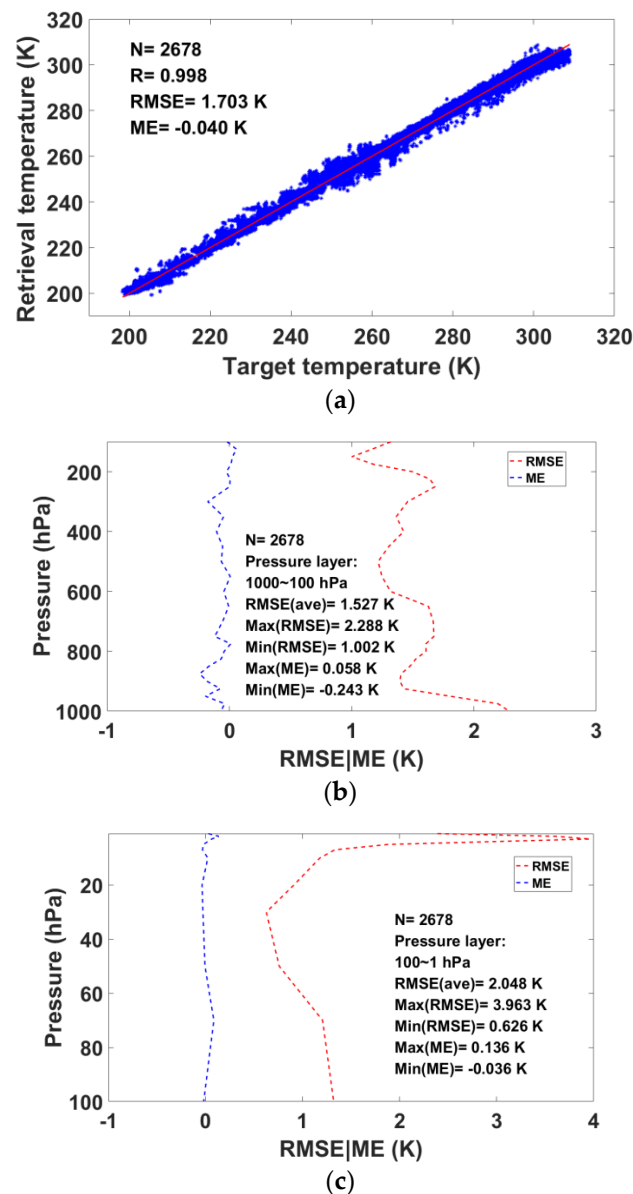


Figure 12. Temperature retrieval results of Method 2: (a) Scatter diagram of temperature retrieval based on Method 2; (b) RMSE and MBE distribution of temperature retrieval in the troposphere based on Method 2; (c) RMSE and MBE distribution of temperature retrieval in the stratosphere based on Method 2.

4.3.2. Relative Humidity Retrieval Results

Figure 13a shows the scatter diagram of the retrieved atmospheric relative humidity. All the data information of the test samples is consistent with the above study. The results indicate that the correlation coefficient between the retrieved relative humidity and target is 0.933. The RMSE of the relative humidity of the whole atmosphere is 9.071%, and the MBE is -0.543% . The retrieved relative humidity is 0.543% lower than the target relative humidity.

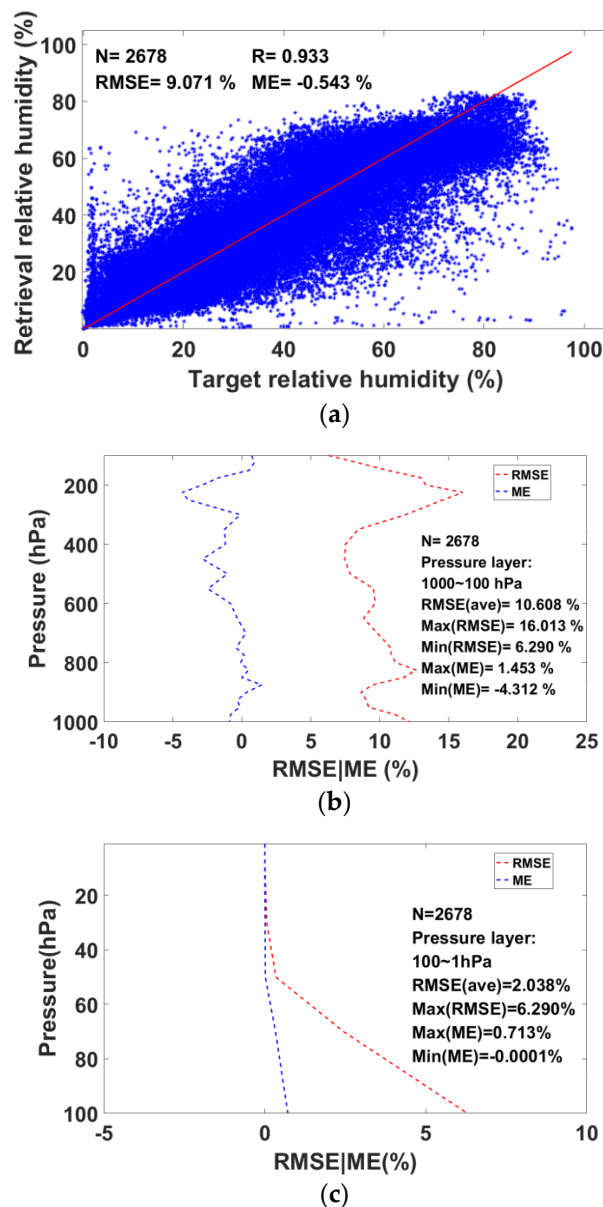


Figure 13. Relative humidity retrieval results of Method 2: (a) Scatter diagram of relative humidity retrieval based on Method 2; (b) RMSE and MBE distribution of relative humidity retrieval in the troposphere based on Method 2; (c) RMSE and MBE distribution of relative humidity retrieval in the stratosphere based on Method 2.

Figure 13b,c show the RMSE and MBE distribution of the relative humidity retrieval in the troposphere and stratosphere. As shown in Figure 13b, the average RMSE in the troposphere is 10.608%. The lowest RMSE occurs at 100 hPa, which is 6.290%. The highest RMSE occurs at 225 hPa, which is 16.013%. The maximum positive deviation is 1.453%, and the maximum negative deviation is -4.312% . As shown in Figure 13c, the average RMSE in the stratosphere is 2.038%, which is significantly low when compared with the RMSE in the troposphere. Similarly, given that the water vapor content in the upper layer is considerably less than that in the surface layer, the relative humidity value in the upper layer is generally low.

4.4. Comparison between Retrieval Results of Method 1 and AIRS Products

In order to further evaluate the retrieval results of the proposed method, the temperature and humidity profiles obtained from the AIRS are employed for further comparisons with the retrieval profiles from the GIIRS using Method 1. The GIIRS data are collected with the AIRS for the same period for comparison with the collection criteria of ± 1 h in time and $\pm 0.25^\circ$ in space. The number of the collected samples used for comparison is 202. Assuming the atmospheric profiles from the AIRS to be the standard profiles, as shown in Figure 14a, the mean bias of the temperature profiles is between -2.767 K and 2.733 K. The maximum positive deviation occurs at around 5 hPa, and the deviation for 10–1000 hPa is within 1 K. In general, the RMSE varies between 0.583 K and 3.152 K; the RMSE in most of the atmospheric layers is within 1.5 K and slightly higher at the top of the stratosphere, with a maximum value of 3.152 K. Meanwhile, the mean bias of the relative humidity profiles is between -3.561% and 15.180% . The maximum positive deviation is recorded at around 250 hPa. The deviation for most layers is within 10%. The RMSE is between 0.668% and 19.832% in general, with the maximum RMSE value recorded at around 300 hPa.

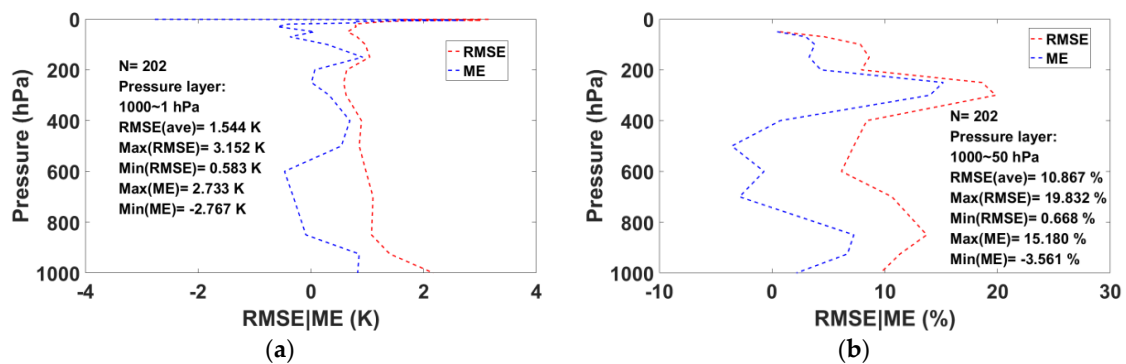


Figure 14. Comparison between the retrieval results of Method 1 and the Atmospheric Infrared Sounder (AIRS) products: (a) the RMSE and mean bias for Temperature; (b) the RMSE and mean bias for relative humidity (AIRS products are denoted as the standard profiles).

Furthermore, the AIRS products and our results are also compared against the ERA-Interim data. Assuming the atmospheric profiles from the ERA-Interim data to be the standard profiles, the results are illustrated in Figure 15. As can be observed from the figure, both the temperature and relative humidity profiles retrieved from the GIIRS are closer to the ERA-Interim data. The temperature bias for the AIRS varies from -2.454 K to 3.001 K, with the maximum positive deviation recorded at around 1 hPa and the maximum negative deviation recorded at around 5 hPa. On the other hand, the maximum positive deviation and the maximum negative deviation for the retrieval results are 0.279 K and -0.475 K, respectively. The temperature RMSE for the AIRS varies from 0.475 K to 3.353 K, with the maximum value at 1 hPa. The temperature RMSE for the retrieval results was between 0.308 K and 1.462 K, while most of the layers are within 1 K. In regard to the humidity comparisons, the AIRS has a negative humidity bias above 400 hPa as well as below 800 hPa; the minimum deviation occurs at 250 hPa and 850 hPa. The humidity biases for the retrieval results of all layers are reported to be within 3%. The trend of the RMSE curves of relative humidity is basically the same, with two change corners near 250 hPa and 850 hPa.

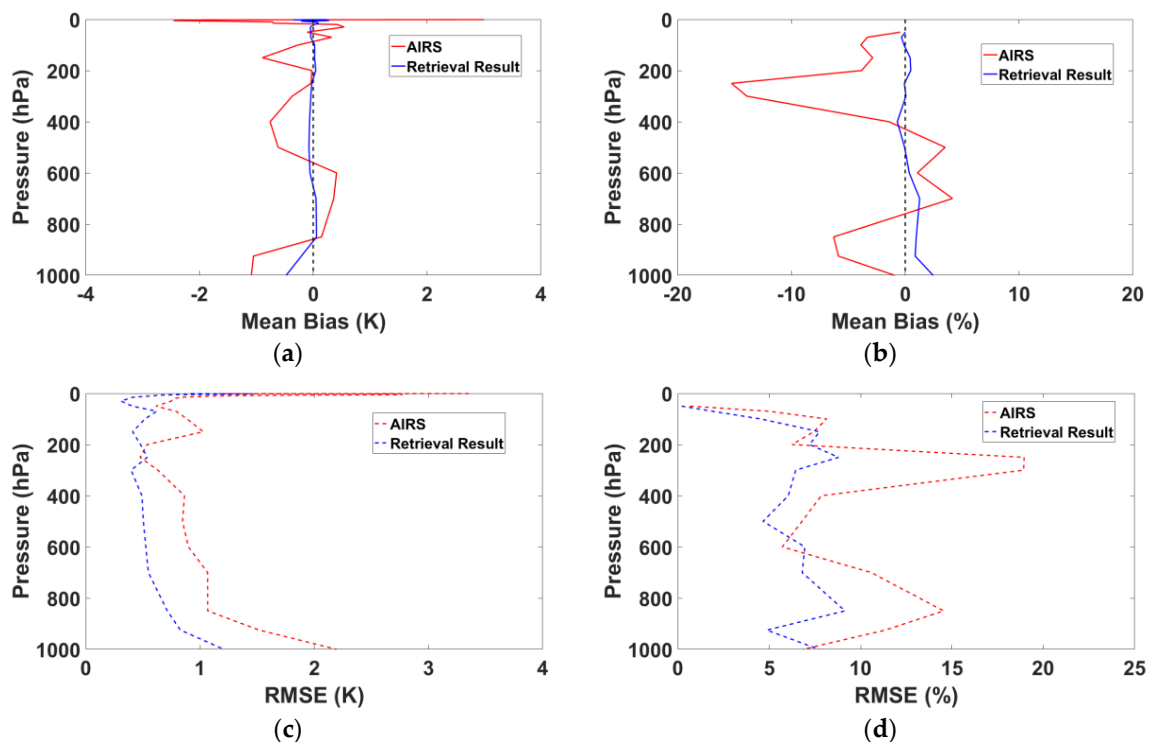


Figure 15. (a,c) The mean bias and RMSE of the temperature profile, respectively; (b,d) The mean bias and RMSE of the humidity profile, respectively (the red solid line and the red dotted line represent the comparison between the AIRS products and the ERA-Interim data, while the blue solid line and the blue dotted line represent the comparison between the retrieval profiles and the ERA-Interim data).

5. Discussion

Compared with other methods, the approach of ANNs used in the study based on the MATLAB platform allowed describing the non-linear relation between radiance and atmospheric variables well without the need for the complex relationships of physical models. Additionally, it is quite convenient to use as it does not need great effort to find a formula for retrieving variables, and it is easy to program and calculate with hardware and software. As one of the machine learning methods, although the construction process for the network requires the support of data samples, after the training is completed, the retrieval process is very convenient, with low hardware requirements and high computational efficiency. At the same time, we can extract the weights and thresholds of each layer from the trained network in MATLAB and formulate the retrieval algorithm according to the extracted parameters, or rewrite the network retrieval algorithm into other programming languages, such as the C language, according to the weights and thresholds of the trained network, so that this algorithm is not limited to a certain platform.

The comparisons of the network retrieval results and ERA-Interim data indicates that the neural network has good prospects in the retrieval of temperature and humidity profiles from the GIIRS based on the FY-4A satellite. In comparison to previous studies of using simulation data to build the network [8], this study proposes a method of directly using EC data and GIIRS observation data to build the network, and goes one step further by comparing the two methods. Additionally, we find that the deviation correction of the measured data is helpful in improving the retrieval accuracy in the method of using simulation data to build the network. Near the surface around 1000 hPa, the radiation received by the satellite comes also from the infrared radiation emitted from the Earth's surface in addition to the radiation from the surface atmosphere. Therefore, compared with the upper atmosphere, the retrieval near the Earth's surface is affected by more factors, which may lead to the network's insufficient learning in this part, resulting in the relatively low retrieval accuracy in this part. The relatively low retrieval accuracy at the top of the stratosphere may be related to the network

parameter settings and the ERA-Interim data themselves. The parameter settings used in the study do not necessarily correspond to the optimal parameter scheme; also, the consistency and stability of the ERA-Interim data themselves at the top of the stratosphere are also factors that need to be considered, and these may bring some errors to the retrieval at the top of the stratosphere. In Method 2, due to the assumption of constant emissivity and other reasons, the model itself will include some errors. At the same time, the step of removing some of the data samples when processing the simulation data will also have a certain impact on the results. In addition, there is still room for improvement in the construction of the correction models, which is not necessarily optimal at present. Considering all these factors, it is relatively difficult for Method 2 to achieve the same retrieval accuracy as Method 1.

A few errors still exist in the BP neural network retrieval model developed in the study. With respect to the retrieval results of the network, the possible causes of these errors include the following:

1. Given the effect of instrument and observation errors, the EC data obtained do not fully represent the distribution of the GIIRS observation data at all altitudes, which is a source of error.
2. The network retrieval accuracy is also affected by the network parameter settings. The parameter settings used in the study do not necessarily correspond to the optimal parameter scheme; this itself inevitably also leads to a prediction error.
3. The accuracy of the clear sky screening cannot be guaranteed as 100%, which also leads to some errors.
4. The satellite observation data do not completely correspond to the EC grid data. In order to obtain time matching with the EC data, the data were collected at 00:00, 06:00 and 12:00 UTC in July–August, 2018 within the 0.5 h time window of the GIIRS observations. Therefore, a few errors may be included in the spatiotemporal matching of data.

The method introduced in the study has significant potential to be adopted for operational implementation in the future. ANNs are relatively insensitive to reasonable uncertainties in the input data. Additionally, ANNs are easy to program and calculate with hardware and software, which makes this proposed method implementation easy. With high computational efficiency and low hardware requirements, the whole retrieval process is very simple and convenient to implement. Compared with the method of using the simulated data to construct the network for temperature and humidity profiles retrieval, our technique is more convenient in regard to the process of network construction, and its implementation process as a whole is more concise. At the same time, it also has a lot of room for improvement and development. With the expansion of the dataset in time and space, the scope of network application will be wider. At present, the retrieval model is only established for the North China Plain in summer and the current model may not be able to well meet the retrieval requirements of areas with more complex terrain as well as in other time periods, due to the representativeness of the samples used in this study. In the future, it will be necessary to add data from other regions and other time periods during the network construction and establish different retrieval models for different areas and time periods so as to meet the real-time retrieval requirements for the nationwide atmospheric temperature and humidity profiles.

6. Conclusions

In the present study is proposed a new technique for retrieving temperature and humidity profiles directly from the combined use of GIIRS L1 and EC reanalysis data based on Artificial Neural Networks (ANNs). This technique is compared against a method widely used in the past for this purpose that is based on simulated data to construct the network for retrievals. The performance of both methods was evaluated by comparison of the retrieval results in the North China Plain in July and August 2018 against the ERA-Interim data. In additional, the retrieval results were also compared with the AIRS products for further evaluation.

The results obtained from this study are summarized as follows:

- When compared with the method that is based on simulated data to construct the network for retrievals, the method proposed in this study is superior in terms of retrieval accuracy during the comparison of the retrieval results. The temperature retrieval RMSE for the troposphere of the two methods can differ by approximately 1 K; the RMSE difference for the stratosphere is approximately 1.2 K.
- The retrieval results for the troposphere exhibit better accuracy and better consistency with the EC data than those for the stratosphere. The RMSE of the retrieved troposphere temperature and relative humidity using the ANN built with the GIIRS L1 and EC data are 0.557 K and 6.003%, respectively.
- The RMSEs of the relative humidity in the complete atmosphere as retrieved by the two sets of networks are both within 10%, while the RMSEs of the relative humidity in the troposphere retrieved by the two sets of networks are 6.003% and 10.608%, respectively.
- A low correlation between the simulated and observed radiance exists in the range of 720–736.875 cm^{-1} and is mainly concentrated in the temperature retrieval band, while the correlation between the simulated and observed radiance of the water vapor channels exceeds that between the temperature channels.
- Compared with AIRS products, the temperature shows great consistency in the troposphere, with the RMSE in most of the atmospheric layers being within 1.5 K, while the relative humidity shows better consistency below 500 hPa. Additionally, the retrieval results of the proposed method are more consistent with the ERA-Interim data than the AIRS products.

Our results demonstrate promising performance on temperature and humidity profile retrieval from GIIRS L1 data using the Artificial Neural Network and have important reference value for GIIRS channel evaluation. The retrieval model is, at present, mainly developed for the North China Plain in July and August in summer, for which its use was also demonstrated. With the high observation frequency (<1 h in the China region) of geostationary satellites, we can obtain high-frequency temperature and humidity profiles using this method in this time period of this area. We also recognize that the GIIRS data used in the study exhibit certain some limitations in the distribution of time and space. However, it has great potential for expansion in multiple directions and also for the operationalization of its implementation. A future study will involve expanding the sample, training different applicable models for different regions and time periods, and systematically evaluating the retrieval accuracy of different retrieval models. With this, we will be able to obtain high-frequency temperature and humidity profiles in more areas and time periods.

Author Contributions: Conceptualization, X.C. and Y.B.; methodology, X.C. and Y.B.; software, X.C.; validation, X.C., F.L. and Q.L.; formal analysis, X.C.; investigation, G.P.P.; resources, F.L. and Q.L.; data curation, L.Z. and Y.W.; writing—original draft preparation, X.C.; writing—review and editing, G.P.P. and Y.B.; visualization, Y.W.; supervision, Y.B.; project administration, Y.B. All authors have read and agreed to the published version of the manuscript.

Funding: This research was funded by the National Key Research and Development Program of China (2017YFC15017043, 2018YFC1407200, 2016YFA0600703), and National Natural Science Foundation of China (41975046).

Acknowledgments: We would like to thank the National Satellite Meteorological Center for sharing FY4A/GIIRS data and giving advice on how to use these data. We also thank the anonymous reviewers for the comments that helped improve our manuscript.

Conflicts of Interest: The authors declare no conflict of interest.

References

1. Bao, Y.S.; Cai, X.; Qian, C.; Min, J.Z.; Lu, Q.F.; Zuo, Q. 0–10 km temperature and humidity profiles retrieval from ground-based microwave radiometer. *J. Trop. Meteorol.* **2018**, *24*, 243–252.
2. Li, J.; Li, J.; Otkin, J.; Schmit, J.T.; Liu, C.-Y. Warning Information in a Preconvection Environment from the Geostationary Advanced Infrared Sounding System-A Simulation Study Using the IHOP Case. *J. Appl. Meteorol. Climatol.* **2011**, *50*, 776–783. [[CrossRef](#)]

3. Guan, Y.H.; Ren, J.; Bao, Y.S.; Lu, Q.F.; Liu, H.; Xiao, X.J. Research of the infrared high spectral (IASI) satellite remote sensing atmospheric temperature and humidity profiles based on the one-dimensional variational algorithm. *Trans. Atmos. Sci.* **2019**, *42*, 602–611. [[CrossRef](#)]
4. Ma, X.L.; Jiang, S.; Yu, Y.M.; Guo, H. Analyzing the quality of data for temperature and humidity using COSMIC radio occultation observations. *Trans. Atmos. Sci.* **2017**, *40*, 841–849. [[CrossRef](#)]
5. King, J.I. The radiative heat transfer of planet earth. In *Scientific Uses of Earth Satellites*; University of Michigan Press: Ann Arbor, MI, USA, 1958; pp. 133–136.
6. Huang, W.; Gao, T.C.; Liu, L. Review of Remote Sensing Retrieval of Temperature and Water Vapor Profiles Using Ground-based Infrared Hyper-spectral Data. *Infrared* **2015**, *1*. [[CrossRef](#)]
7. Dong, C.H.; Li, J.; Zhang, P. *Principle and Application of Hyperspectral Infrared Remote Sensing of Atmosphere*; Beijing Science Press: Beijing, China, 2013.
8. Bao, Y.S.; Wang, Z.J.; Chen, Q.; Zhou, A.M.; Dong, Y.H.; Min, J.Z. Preliminary Study on Atmospheric Temperature Profiles Retrieval from GIIRS Based on FY-4A Satellite. *Aerosp. Shanghai* **2017**, *34*, 28–37. [[CrossRef](#)]
9. Dong, Y.H. FY-4 Meteorological Satellite and Its Application Prospect. *Aerosp. Shanghai* **2016**, *33*, 1–8.
10. Yang, J.; Zhang, Z.; Wei, C.; Lu, F.; Guo, Q. Introducing the new generation of Chinese geostationary weather satellites, Fengyun-4. *Bull. Am. Meteorol. Soc.* **2017**, *98*, 1637–1658. [[CrossRef](#)]
11. Di, D.; Li, J.; Han, W.; Bai, W.; Wu, C.; Menzel, W.P. Enhancing the Fast Radiative Transfer Model for FengYun-4 GIIRS by Using Local Training Profiles. *J. Geophys. Res. Atmos.* **2018**, *123*. [[CrossRef](#)]
12. Hua, J.W.; Mao, J.H. “No.4 Feng Yun” Meteorological Satellite Atmospheric Vertical Sounder. *Science* **2018**, *70*, 24–29. [[CrossRef](#)]
13. Guan, L. A Study on Infrared Hyperspectral Measurements and Its Applications on Cloud Detection, Cloud-Clearing and Atmospheric Sounding Profile. Ph.D. Thesis, Nanjing University of Information Science&Technology, Nanjing, China, 2005.
14. Jiang, D.M.; Dong, C.H.; Lu, W.S. Preliminary Study on the Capacity of High Spectral Resolution Infrared Atmospheric Sounding Instrument Using AIRS Measurements. *J. Remote Sens.* **2006**, *10*, 586–592.
15. Liu, H. Preliminary Study on Atmospheric Temperature Profile Retrieval Using Atmospheric Infrared Sounder (AIRS). Master’s Thesis, Chinese Academy of Meteorological Sciences, Beijing, China, 2006.
16. Ma, P.F.; Chen, L.F.; Tao, J.H.; Su, L.; Tao, M.H.; Wang, Z.F.; Zou, M.M.; Zhang, Y. Simulation of Atmospheric Temperature and Moisture Profiles Retrieval from CrIS Observations. *Spectrosc. Spectr. Anal.* **2014**, *34*, 1894–1897. [[CrossRef](#)]
17. Guan, L.; Liu, Y.; Zhang, X.H. Application of Artificial Neural Network Algorithm in Retrieving Atmospheric Temperature Profiles from Hyperspectral Infrared Data. *Trans. Atmos. Sci.* **2010**, *33*, 341–346. [[CrossRef](#)]
18. Jiang, D.M.; Cao, S.Q.; Qu, Y.M. A Neural Networks Approach to Retrieval of Atmospheric Temperature Profile from High Spectral Resolution Infrared Measurements. *J. Trop. Meteorol.* **2010**, *26*, 819–824.
19. Shi, L.; Matthews, J.L.; Ho, S.-P.; Yang, Q.; Bates, J.J. Algorithm development of temperature and humidity profile retrievals for long-term HIRS observations. *Remote Sens.* **2016**, *8*, 280. [[CrossRef](#)]
20. Blackwell, W.J.; Chen, F.W. Neural network retrieval of atmospheric temperature and moisture profiles from AIRS/AMSU data in the presence of clouds-art. no. 62331E. In Proceedings of the SPIE—The International Society for Optical Engineering, Orlando, FL, USA, 17–21 April 2006; Volume 6233. [[CrossRef](#)]
21. Wang, Y.; Wang, Z.H.; Li, Q.; Zhu, Y.Y. Research of the one-dimensional variational algorithm for retrieving temperature and humidity profiles from the ground-based microwave radiometer. *Acta Meteorol. Sin.* **2014**, *72*, 570–582. [[CrossRef](#)]
22. Guan, Y.H.; Zhou, G.Q.; Lu, W.S.; Chen, J.P. Theory Development and Application of Data Assimilation Methods. *Meteorol. Disaster Reduct. Res.* **2007**, *30*, 938–950.
23. Bi, Y.M.; Liao, M.; Zhang, P.; Ma, G. 1DVAR retrieval method for GPS radio occultation measurements of atmospheric temperature and humidity profiles. *Acta. Phys. Sin.* **2013**, *62*, 576–582. [[CrossRef](#)]
24. Wang, Z.; Li, Q.; Hu, F.; Cao, X.; Chu, Y. Remote sensing of lightning by a ground-based microwave radiometer. *Atmos. Res.* **2014**, *150*. [[CrossRef](#)]
25. Zheng, F.B.; Zhou, Z.C.; Liu, Y.; Zuo, X.Y.; Zhu, W.D. Temporal and Spatial Distribution Characteristics of Long-term Aerosol Optical Depth in North China Plain Based on MODIS Data. *J. Henan Univ. (Nat. Sci.)* **2019**, *49*, 450–458.
26. Zhang, W.T.; Zhang, X.Y.; Liu, L.; Zhao, L.M.; Lu, X.H. Spatial variations in NO₂ trend in North China Plain based on multi-source satellite remote sensing. *J. Remote Sens.* **2018**, *22*, 335–346. [[CrossRef](#)]

27. Wang, X.H.; Su, L.; Tao, M.H.; Wang, Z.F.; Chen, L.F.; Li, S.S.; Wang, Y. A study of winter haze pollution over a rural area of central Northern China Plain based on satellite and surface observations. *China Environ. Sci.* **2016**, *36*, 1610–1620. [[CrossRef](#)]
28. An, X.D.; Zhang, J.H.; Liu, X.F.; Yao, F.M. Aerosol detection analysis from satellite during the harvest season over North China Plain. *Acta Sci. Circumstantiae* **2016**, *36*, 3386–3392. [[CrossRef](#)]
29. Chen, R.; Gao, C.; Wu, X.W.; Zhou, S.Y.; Hua, J.W.; Ding, L. Application of FY-4 atmospheric vertical sounder in weather forecast. *J. Infrared Millim. Waves* **2019**, *38*, 285–289.
30. Hu, J.Y.; Tang, S.H.; Dong, L.X. Land Surface Temperature Retrieval from FY3A/MERSI. *Remote Sens. Technol. Appl.* **2014**, *29*, 531–538. [[CrossRef](#)]
31. Hannon, S.E.; Strow, L.L.; Mcmillan, W.W. Atmospheric Infrared Fast Transmittance Models: A Comparison of Two Approaches. *Proc. SPIE* **1996**, 2830. [[CrossRef](#)]
32. Blackwell, W.J. A neural-network technique for the retrieval of atmospheric temperature and moisture profiles from high spectral resolution sounding data. *IEEE Trans. Geosci. Remote Sens.* **2005**, *43*, 2535–2546. [[CrossRef](#)]
33. Blackwell, W.J.; Chen, F.W. *Neural Networks in Atmospheric Remote Sensing*; Artech House, Institute of Technology: Norwood, MA, USA, 2009.
34. Zheng, G.; Yang, J.S.; Li, X.F.; Zhou, L.Z.; Ren, L.; Chen, P.; Zhang, H.G.; Lou, X.L. Using artificial neural network ensembles with crogging resampling technique to retrieve sea surface temperature from hy-2a scanning microwave radiometer data. *IEEE Trans. Geosci. Remote Sens.* **2018**, *57*, 985–1000. [[CrossRef](#)]
35. Sit, H.; Earls, C.J. Characterizing Evaporation Ducts Within the Marine Atmospheric Boundary Layer Using Artificial Neural Networks. *Radio Sci.* **2019**, *54*, 1181–1191. [[CrossRef](#)]
36. Shalev-Shwartz, S.; Ben-David, S. *Understanding Machine Learning: From Theory to Algorithms*; Cambridge University Press: New York, NY, USA, 2014. [[CrossRef](#)]
37. Zhu, T.; Huang, Y.; Wei, H. Estimating Climate Feedbacks Using a Neural Network. *J. Geophys. Res. Atmos.* **2019**, *124*, 3246–3258. [[CrossRef](#)]
38. Sauzède, R.; Claustre, H.; Jamet, C.; Uitz, J.; Ras, J.; Mignot, A.; D’Ortenzio, F. Retrieving the vertical distribution of chlorophyll a concentration and phytoplankton community composition from in situ fluorescence profiles: A method based on a neural network with potential for global-scale applications. *J. Geophys. Res. Ocean.* **2015**, *120*, 451–470. [[CrossRef](#)]
39. Zhang, Z.H. Artificial Neural Network. In *Multivariate Time Series Analysis in Climate and Environmental Research*; Springer International Publishing: Cham, Switzerland, 2018; pp. 1–35. [[CrossRef](#)]
40. Milstein, A.B.; Blackwell, W.J. Neural network temperature and moisture retrieval algorithm validation for AIRS/AMSU and CrIS/ATMS. *J. Geophys. Res. Atmos.* **2016**, *121*, 1414–1430. [[CrossRef](#)]
41. Papale, D.; Black, T.A.; Carvalhais, N.; Cescatti, A.; Chen, J.; Jung, M.; Kiely, G.; Lasslop, G.; Mahecha, M.D.; Margolis, H.; et al. Effect of spatial sampling from European flux towers for estimating carbon and water fluxes with artificial neural networks. *J. Geophys. Res. Biogeosci.* **2015**, *120*, 1941–1957. [[CrossRef](#)]
42. Krasnopolsky, V.M. Neural network emulations for complex multidimensional geophysical mappings: Applications of neural network techniques to atmospheric and oceanic satellite retrievals and numerical modeling. *Rev. Geophys.* **2007**, *45*. [[CrossRef](#)]
43. Ma, H.Z. The Research and Application on BP Neural Network. Master’s Thesis, Northeast Agricultural University, Heilongjiang, China, 2015.
44. Sharifi, E.; Saghafian, B.; Steinacker, R. Downscaling Satellite Precipitation Estimates with Multiple Linear Regression, Artificial Neural Networks, and Spline Interpolation Techniques. *J. Geophys. Res. Atmos.* **2019**, *124*, 789–805. [[CrossRef](#)]
45. Yang, Y.; Shen, F.; Yang, Z.C.; Feng, X.S. Prediction of Solar Wind Speed at 1 AU Using an Artificial Neural Network. *Space Weather* **2018**, *16*, 1227–1244. [[CrossRef](#)]
46. Sauzède, R.; Claustre, H.; Uitz, J.; Jamet, C.; Dall’Olmo, G.; D’Ortenzio, F.; Gentili, B.; Poteau, A.; Schmechtig, C. A neural network-based method for merging ocean color and Argo data to extend surface bio-optical properties to depth: Retrieval of the particulate backscattering coefficient. *J. Geophys. Res. Ocean.* **2016**, *121*, 2552–2571. [[CrossRef](#)]
47. Pasini, A. Artificial neural networks for small dataset analysis. *J. Thorac. Dis.* **2015**, *7*, 953. [[CrossRef](#)]
48. Liu, T.S. The Research and Application on BP Neural Network Improvement. Master’s Thesis, Northeast Agricultural University, Heilongjiang, China, 2011.

49. Liu, Y. A Study on the Retrieval of Clear-sky Atmospheric Humidity Profiles Using Artificial Neural Network Algorithm. Master's Thesis, Nanjing University of Information Science and Technology, Nanjing, China, 2011.
50. Wang, B. Research on Remote Sensing Atmospheric Environment Measured by Ground-based Microwave Radiometer. Master's Thesis, Ocean University of China, Shangdong, China, 2007.
51. Zhang, Q.L.; Li, X.M. A New Method to Determine Hidden Note Number in Neural Network. *J. Jishou Univ. Nat. Sci.* **2002**, *23*, 89–91.
52. Jiao, B. Determination of Hidden Unit Number in a BP Neural Network. *J. Shanghai Dianji Univ.* **2013**, *16*.
53. Ishimoto, H.; Okamoto, K.; Okamoto, H.; Sato, K. One-dimensional variational (1D-Var) retrieval of middle to upper tropospheric humidity using AIRS radiance data. *J. Geophys. Res. Atmos.* **2014**, *119*. [[CrossRef](#)]



© 2020 by the authors. Licensee MDPI, Basel, Switzerland. This article is an open access article distributed under the terms and conditions of the Creative Commons Attribution (CC BY) license (<http://creativecommons.org/licenses/by/4.0/>).